

**NASA
Technical
Paper
3333**

June 1993

**Effect of Pylon Cross-Sectional
Geometries on Propulsion
Integration for a
Low-Wing Transport**

Anthony M. Ingraldi,
Dinesh A. Naik,
and Odis C. Pendergraft, Jr.

**NASA
Technical
Paper
3333**

1993

**Effect of Pylon Cross-Sectional
Geometries on Propulsion
Integration for a
Low-Wing Transport**

Anthony M. Ingraldi
*Langley Research Center
Hampton, Virginia*

Dinesh A. Naik
*ViGYAN, Inc.
Hampton, Virginia*

Odis C. Pendergraft, Jr.
*Langley Research Center
Hampton, Virginia*

Summary

Pylon cross-sectional geometries that are intended to improve the aerodynamics of the propulsion system installation were investigated on a 1/17th-scale, low-wing transport model in the Langley 16-Foot Transonic Tunnel. The basic design philosophy for these pylons was to alleviate flow acceleration without introducing severe adverse pressure gradients near the pylon-wing junction. This result was achieved by means of a gradually diverging pylon with the maximum thickness occurring at the wing trailing edge. The pylon closure occurred aft of the wing trailing edge. Other pylon cross-sectional geometries were also tried, but only the pylon design described above and its hybrid derivative achieved the desired result. The force data, surface static pressure measurements, and surface flow visualization data that were obtained support this result. Data were taken at Mach numbers from 0.50 to 0.80, model angles of attack from -4° to 6° , and pylon toe-in angles from 0° to 3° .

Introduction

Propulsion integration for transport aircraft has been a priority area in aerodynamic research and will continue to play a crucial role in the development and marketing of new-generation aircraft. Reductions in installed drag on the order of 1 percent of total aircraft drag can translate into substantial financial savings to airline operators. Some aspects of propulsion integration that can be studied in order to reduce the drag penalty associated with engine installation are the proximity of the engine nacelle to the wing, the spanwise location of the engine-pylon combination, pylon geometry, and the type of installation (i.e., under the wing, over the wing, or fuselage mounted).

This study is part of an ongoing research program in transport propulsion integration at the NASA Langley Research Center. The configuration used in this study is a 1/17th-scale, low-wing transport aircraft with pylons installed under the wings. The aircraft has a supercritical wing section and is designed for a cruise lift coefficient of 0.55 at a Mach number of 0.77. Interference effects of flow-through nacelles under the wings with bypass ratios of 6 and 18 have been previously investigated on this model (refs. 1, 2, and 3). Computational fluid dynamic analysis of the fuselage-wing-pylon-nacelle geometry has also been performed with an Euler code (ref. 4). The current study concentrates on pylon-alone installations. The eventual goal is to unify the lessons learned from pylon-alone studies with those from pylon-

nacelle studies and produce a design methodology for propulsion integration.

The impetus behind the current pylon cross-sectional geometry study is the added flow acceleration and consequent lift loss caused by the installation of the pylon-nacelle assembly on the wing lower surface. Pressure contours of the wing lower surface were computed (ref. 4) with an Euler code for the complete aircraft, i.e., for the fuselage, wing, pylon, and nacelle. The results, which were in reasonable agreement with experimental pressure data (ref. 1), indicated high flow velocities induced on the wing lower surface by the flow accelerating around the thickest portion of the pylon. This effect may have been compounded by the fact that the maximum thickness of the pylon occurred near the maximum thickness of the supercritical wing. These low pressures resulted in a loss of lift.

Farther aft, adverse pressure gradients were imposed on the wing lower surface because the flow compressed as it traversed the pylon trailing-edge closure region. These adverse gradients could have resulted in flow separation in this region with a consequent increase in drag. An example of this type of flow separation is shown in figure 1 where prominent features are labeled. Here a flow-through nacelle representing an engine with a bypass ratio of 6 (refs. 1, 2, and 3) was mounted at a nondimensional spanwise wing station (η) of 0.340 on the model. The large separation region, indicated by fluorescent oil pooled at the separation line, demonstrates that improvement is needed in the pylon design. (Note that the dark patch on the forward portion of the inboard wing lower surface is from a shadow thrown by the pylon-nacelle assembly.)

These problems are believed to be avoidable with a flat-sided pylon of increasing thickness whose closure is moved aft of the wing trailing edge while maintaining the pylon maximum thickness. In order to minimize the adverse effects, the pylon should be widest at the wing trailing edge (ref. 5). This type of pylon is called a *compression pylon*. The compression pylon is expected to have higher skin-friction drag than a conventional partial-chord pylon because of its larger wetted area. However, at cruise this effect can be more than offset by lower interference drag.

The compression pylon design can be further refined by varying the toe-in angle and also by tailoring the outboard side of the pylon differently from the inboard side to accommodate any cross flow arising from wing sweep and fuselage blockage. In this paper, the latter geometry is referred to as a *hybrid pylon*. The earlier pylon-nacelle studies (ref. 3) have

shown that the changes in pylon toe-in angle, though for the most part minimally effective, can sometimes result in lower installation drag.

The current investigation was conducted to compare the installation effect of various pylon geometries versus the wing without pylons (clean wing) in terms of the distributions of wing surface pressure coefficient, the amount of flow separation at the pylon-wing junction, and the aerodynamic force characteristics of the transport model.

Symbols and Abbreviations

BL	buttlane, in.
b	wingspan, in.
C_L	lift coefficient, $Lift/q_\infty S$
C_p	static pressure coefficient, $(p - p_\infty)/q_\infty$
c	local wing chord, in.
c_n	section normal-force coefficient
c'	local pylon chord (defined to be $0.95c$), in.
\bar{c}	mean aerodynamic chord, in.
FS	fuselage station, in.
M	Mach number
p	static pressure, lb/in ²
q	dynamic pressure, lb/in ²
S	wing reference area, in ²
WL	waterline, in.
WRP	wing reference plane
x	local pylon ordinate, in.
y	local pylon coordinate, in.
α	angle of attack, deg
η	nondimensional spanwise wing station
Subscripts:	
des	design point
∞	free-stream condition

Apparatus and Procedure

Wind Tunnel and Model Support

The present investigation was conducted in the Langley 16-Foot Transonic Tunnel. This facility is a

single-return, continuous-flow atmospheric wind tunnel with a test section of octagonal cross section and a throat cross-sectional area of 199.15 ft². The 31-ft-long test section (the maximum length at subsonic speeds) has slots located at the corners of the octagon that vent the test section to a surrounding plenum to provide transonic capability. The test section airspeed is continuously adjustable between Mach numbers of 0.20 and 1.30 with an accuracy of ± 0.005 . The wall divergence in the test section is adjusted as a function of the airstream dew point and Mach number to minimize any longitudinal static pressure gradients in the test section. No wall divergence is necessary below a Mach number of 0.825. The model was sting mounted and held near the test section centerline at all angles of attack by the support-system arrangement. Further information on the wind tunnel and model support equipment can be found in references 6 and 7.

Model

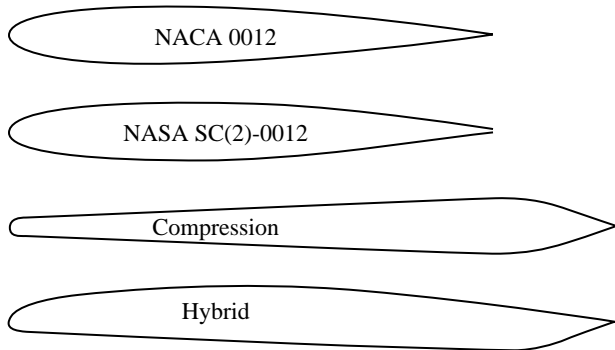
The sketch in figure 2(a), which shows the basic research transport model in the clean wing configuration (without pylons), includes the overall dimensions and important geometric parameters. The photograph in figure 2(b) shows a front view of the clean wing model. This model is a 1/17th-scale representation of a 150-passenger, twin-engine transport designed to cruise at $M_\infty = 0.77$ and $C_L = 0.55$. Further information about the geometry of the model, in addition to that given below, may be found in reference 1.

Fuselage. The fuselage is 80 in. long, has a maximum diameter of 9.0 in., and is comprised of an ellipsoidal nose profile with circular cross sections, a cylindrical midsection, and an afterbody of elliptical cross sections with vertical major axes.

Wing. The planform geometry of the wing (see fig. 2(c)) has a span of 79.668 in., an aspect ratio of 10.795, a taper ratio of 0.275, and a quarter-chord sweep of 21°. The quarter-chord dihedral of the wing reference trapezoid is 5.78°. Airfoil ordinates and design information for the supercritical wing and wing-fuselage fairing can be found in reference 1.

Pylons. Four different pylon cross sections were studied. These were the NACA 0012, the NASA SC(2)-0012, the compression, and the hybrid cross sections. The pylon cross sections are shown in sketch A. The NASA SC(2)-0012 airfoil is designed specifically for transonic flow regimes in an attempt to improve the performance of the conventional 12-percent-thick airfoil (ref. 8). The two 0012 pylons were nearly full wing-chord pylons. As shown

in figure 3(a), all pylons were set back from the wing leading edge by 5 percent of the local wing chord. For all pylons, the maximum thickness was defined relative to the local NACA 0012 pylon chord. The photographs in figures 3(b) and 3(c) show front and rear views, respectively, of the model with the compression pylons installed, whereas the photograph in figure 3(d) shows a close-up view from below the same pylons.



Sketch A

The compression and the hybrid pylons extended beyond the wing trailing edge but had approximately the same maximum dimensional thickness as the NACA 0012 pylons. The hybrid pylon, with an inboard compression side and an outboard modified NACA 0012 side, was expected (ref. 9) to provide a compromise wing pressure distribution closest to the clean wing pressure distribution. Table I lists the coordinates of the four pylon cross sections.

Two sets of pylons were constructed for each cross section. One set of pylon pairs was sized with respect to the local wing chord for installation at the $\eta = 0.340$ location. The other set was sized for installation at the $\eta = 0.400$ location. The outboard location ($\eta = 0.400$) was a possible alternative location for a higher bypass ratio engine that might not have sufficient ground clearance at $\eta = 0.340$. The photographs of figure 3 show the pylons at $\eta = 0.340$. The pylons were tested without the nacelles attached.

Instrumentation

Forces and moments were obtained on the completely metric model from an internal, six-component strain gauge balance. The longitudinal location of the balance moment center was slightly aft of the quarter-chord of the wing mean aerodynamic chord. (See fig. 2(a).) The model angle of attack was measured by using an accelerometer mounted in the model nose. More than 300 surface pressure orifices

were located on the left wing. The spanwise location of each orifice row is shown in figure 4. The orifices on the lower surface were concentrated in the vicinity of the pylon installation locations of $\eta = 0.340$ and 0.400 so that local flow phenomena around the pylons could be examined in greater detail. All pressure measurements on the wing were made by electronically scanning pressure modules mounted inside the hollow, removable nose section of the model. Each module contained 32 individual pressure transducers capable of transmitting data simultaneously. Further details of this instrumentation can be found in reference 1. The pylons were not instrumented.

Tests

The tests were conducted over a Mach number range from 0.50 to 0.80. This corresponds to a Reynolds number range from 2.0×10^6 to 2.7×10^6 based on the wing mean aerodynamic chord. The angle-of-attack range was from -4° to 6° . Aerodynamic force and pressure data were obtained for the clean wing model shown in figure 2 and for the model with the pylon configurations installed. Four different pylon toe-in angles (nominally 0° , 1° , 2° , and 3°) were investigated for each pylon tested. Toe-out angles were not investigated. Transition grit strips were located on the model based on the observations from oil flow studies on the clean wing (ref. 1). Locations for the transition grit on the wing, fuselage, and pylon are given in figures 5(a), 5(b), and 5(c), respectively. A fluorescent oil flow technique was employed to obtain flow visualization on the wing in the vicinity of the pylons to determine the extent of flow separation in this region.

Data Reduction

Standard aerodynamic force and moment coefficients were computed using the methods and equations of reference 10. The trapezoidal planform areas of the wing and mean aerodynamic chord were used as the reference area and length, respectively. Resulting model force and moment coefficients were referred to the stability axis system with the moment reference center located at the quarter-chord of the wing mean aerodynamic chord (FS 41.902).

The model angle of attack was computed by correcting the values from the onboard accelerometer for wind tunnel upflow, which was determined from clean wing tests of upright and inverted models. Sting-cavity and fuselage-base pressure measurements were used to correct the axial-force data to the condition of free-stream static pressure acting on the fuselage base and in the sting cavity.

Results and Discussion

The effects of the pylon installations will be discussed in terms of the distributions of the wing pressure coefficients that were measured as well as the lift characteristics of the various configurations. Drag data will not be included in the discussion because its accuracy is questionable. Several flow visualization photographs will be considered as well.

Effect of Pylons Installed at $\eta = 0.340$

The effect of toe-in angle on the lift characteristics of the four pylons installed at $\eta = 0.340$ is shown in figure 6. The variation in pylon toe-in angle had a small effect on lift for all the pylon installations over the full range of test Mach numbers. Figure 7 further illustrates the minimal effect of pylon toe-in angle for data near $M_\infty = 0.77$ and $C_L = 0.55$, the wing design condition. Here the lift curves are presented on a more precise scale near the cruise condition. The smallest divisions on the lift and angle-of-attack axes represent the accuracy of the lift and angle-of-attack measurements, respectively; i.e., $\Delta C_L = \pm 0.01$ and $\Delta \alpha = \pm 0.01^\circ$. Differences in measurements greater than two axis divisions are significant. This criterion leads to the conclusion that all toe-in angles tested for each pylon installation produce essentially the same level of lift for a given angle of attack. The remainder of the discussion will consider only the pylon cross section without regard to the pylon toe-in angle.

Figure 8 compares the lift characteristics at $M_\infty = 0.77$ for each of the pylons installed at $\eta = 0.340$ and for the clean wing. Figure 9, which shows data near the design lift point for the same Mach number on a larger scale, indicates that the compression pylon installation results in the lowest lift loss relative to the clean wing. The hybrid and NASA SC(2)-0012 pylon installations perform essentially the same, whereas the NACA 0012 configuration results in the greatest loss in lift of all the configurations tested.

Figures 10 through 13 show the surface static pressure coefficients at the clean wing design condition for each of the pylon installations. The clean wing pressure coefficients are represented by the dotted lines. (No symbols are shown for the clean wing data for clarity.) The pressure data for the upper surface of the wing show that the compression pylon installation has only a slight effect on the upper surface flow (fig. 12(a)). For the compression pylon installation, the local velocity increases, as indicated by a higher negative C_p peak, for the first 20 percent of the wing chord at $\eta = 0.340$. The compression pylon installation also has the lowest effect on the static

pressure distribution of the wing lower surface, as can be seen in figures 10(b) through 13(b).

The NACA 0012 pylon installation (fig. 10(a)) had the greatest influence on the surface static pressures on the wing upper surface because an angle-of-attack increase of about 0.22° relative to the clean wing was required with the NACA 0012 pylons installed to achieve the design lift condition. This angle-of-attack increase was necessitated by the acceleration of the lower surface flow as indicated in figure 10(b), which shows that the strongest effect of the NACA 0012 pylon installation was measured at the $\eta = 0.310$ location as indicated by the increased negative C_p coefficients. More negative pressure coefficients here indicate a local lift loss which had to be countered by an increase in model angle of attack to achieve the desired lift. An adverse effect of this angle-of-attack increase is seen in the pressure coefficient distribution on the upper surface at $\eta = 0.550$ (fig. 10(a)), where evidence is seen of a shock occurring at about 60 percent of the local wing chord.

The levels of pressure coefficient distributions (C_p) for the NASA SC(2)-0012 and hybrid pylon installations fall between the levels for the compression and NACA 0012 pylon installations. The upper surface C_p levels for the NASA SC(2)-0012 installation were slightly more negative than those for the hybrid pylon installation over much of the wing surface. This change is largely a result of the fact that the data for the NASA SC(2)-0012 installation are for a lift coefficient of 0.56, whereas the data for the hybrid installation are for a lift coefficient of 0.54. The lower surface C_p distributions are less sensitive to small variations in model lift coefficient, which allows a meaningful comparison to be made here. Recall that figure 9 showed that the NASA SC(2)-0012 and hybrid pylon installations resulted in essentially the same lift performance at the cruise condition. Even though the overall effect of these two installations was similar, figures 11(b) and 13(b) indicate that the local effects of the individual pylons were noticeably different. For the NASA SC(2)-0012 pylon installation, the greatest disturbance to the flow is seen at the $\eta = 0.310$ location. A relatively sharp negative C_p peak occurs at about 35 percent of the local wing chord, and separation may be indicated by the flattening of the C_p distribution between 50 and 75 percent of the local wing chord. Measurements for the hybrid pylon installation do not show a severe negative pressure peak or any indication of flow separation, but as can be seen in figure 13(b), the hybrid pylon installation did cause a slight shift toward

more negative pressure coefficients on the wing lower surface between $\eta = 0.277$ and 0.428 .

Figures 14 through 17 show the C_p distributions on the wing lower surface at $\eta = 0.310$ and 0.375 . For a free-stream Mach number of 0.50 (fig. 14), the C_p distributions for the pylon installations do not reflect any severe effects such as the formation of shocks or separation. At this Mach number, the most notable effects on the flow are the more negative pressures induced by the NACA 0012 and NASA SC(2)-0012 pylon installations at $\eta = 0.310$. As Mach number is increased, the effects of the various pylon installations become more distinct. Figure 16(a) shows that at $M_\infty = 0.77$ and $\eta = 0.310$, the NACA 0012 pylon induced the sharpest gradients on the wing, and both the NACA 0012 and NASA SC(2)-0012 pylons may have caused separation as indicated by the leveling off of the C_p distribution between about 60 and 80 percent of the local wing chord. At $M_\infty = 0.80$ (fig. 17), similar effects occur again at $\eta = 0.310$ but to a greater extent. On the outboard side of the pylon ($\eta = 0.375$), the compression pylon had the smallest effect on the wing surface pressures for $x/c < 0.5$. At Mach numbers up to 0.77 , the outboard pressures for the compression pylon installation are virtually the same as those for the clean wing. Beyond the peak value, the C_p distributions for the NACA 0012 pylons are closest to those of the clean wing, which suggests that the outboard sides of the compression and hybrid pylons can be modified for optimum performance.

The pressure data indicated various flow features including separation. Flow visualization was used to determine whether these regions of separation were actually present. Figure 18 shows photographs of fluorescent oil flow visualization on the wing lower surface for $M_\infty = 0.50$ and $C_L = 0.55$. In figure 18(a) the lower surface flow on the clean wing is shown to be fully attached at $\alpha = 1.5^\circ$. The transition grit is indicated in the photograph by the white line running from root to tip. Figures 18(b) and 18(c) show the effects of the NASA SC(2)-0012 and compression pylons on the flow field of the wing lower surface at $\alpha = 1.8^\circ$ and $\alpha = 1.6^\circ$, respectively. A comparison of these two figures shows that the NASA SC(2)-0012 pylon installation perturbed the local flow more than the compression pylon installation. The separation region (not to be confused with the shadow thrown from the pylon on the inboard part of the wing) toward the aft end of the pylon near the pylon-wing junction is larger for the NASA SC(2)-0012 pylon than for the compression pylon.

Figure 19 shows photographs of flow visualization for the wing upper surface for $M_\infty = 0.77$ and

$C_L = 0.55$. Flow separation occurs near the trailing edge of the wing from the wing root out to about the 40-percent wing-semispan location. The different pylons installed at $\eta = 0.340$ produced only slightly different effects on the wing upper surface flow. Flow visualization photographs for the wing lower surface at $M_\infty = 0.77$ are shown in figure 20, where figure 20(b) clearly shows large regions of flow separation on both the inboard and outboard sides of the NASA SC(2)-0012 pylon. A comparison of figure 20(b) with the flow visualization shown in figure 20(c) for the compression pylon installation reveals why the compression pylon has a better lift performance. Figure 20(c) shows that the compression pylon has a relatively small effect on the nature of the flow on the wing lower surface. The pressure distributions of the wing lower surface presented earlier indicate that the NACA 0012 and hybrid pylons perturb the wing flow in a manner similar to that of the NASA SC(2)-0012 and compression pylons, respectively. The NACA 0012 and hybrid pylons are expected to result in wing lower surface separations similar to those for the NASA SC(2)-0012 and compression pylons, respectively.

Figure 21 shows how the wing loading varied along the span for each of the pylons installed at $\eta = 0.340$ and for the clean wing. The data for the compression pylon installation are nearly the same as the data for the clean wing configuration. A slight loss in section normal force for the compression pylon installation is evident at the $\eta = 0.400$ station. The other pylon installations caused a much larger loss in section lift at $\eta = 0.400$. As a consequence of the higher losses near the pylon location, the model was required to be at a higher angle of attack to maintain the desired overall lift. This increase in angle of attack caused the outboard portion of the wing to be more heavily loaded. This load increase implies a structural weight penalty and may introduce outboard shocks on the wing upper surface that can result in an increase in model drag.

Effect of Pylons Installed at $\eta = 0.400$

In addition to the pylons installed at $\eta = 0.340$, data were obtained for the pylons installed at $\eta = 0.400$. Figures 22 through 32 contain data relative to the pylons installed at $\eta = 0.400$. Figure 22 shows the lift characteristics of the clean wing and the pylon-installed configurations for $M_\infty = 0.77$. The data indicate that the NACA 0012 and NASA SC(2)-0012 pylon installations reduced the lift-curve slope relative to the clean wing. The compression and hybrid pylon installations reduce the level of lift for a given angle of attack but maintain nearly the same

lift-curve slope as the clean wing. (This effect was also observed for the $\eta = 0.340$ installations (fig. 8).) Figure 23 shows the lift data for the same condition as that in figure 22, but on a more precise scale. The compression pylon installation at $\eta = 0.400$ had the least effect on the angle of attack required to achieve a given level of lift, as was also the case at $\eta = 0.340$.

Figures 24 through 27 depict the static pressure coefficients on the wing surface at the cruise condition for the four pylons installed at $\eta = 0.400$. The dotted lines in the figures represent the clean wing data. Flow features similar to those found in figures 10 through 14 for $\eta = 0.340$ can be seen in the data for the $\eta = 0.400$ installations as well. In particular, regions of separation apparently exist on the inboard sides of the NASA SC(2)-0012 and NACA 0012 pylons. Additionally, the static pressure distribution associated with the compression pylon installation is nearest the clean wing pressure distribution, which is in agreement with the lift data shown in figures 22 and 23.

Figures 28 through 31 show the static pressure coefficients on the lower surface of the wing for the measurement locations nearest the inboard and outboard sides of the pylon. In general, the compression pylon installation caused the smallest departure from the clean wing pressure levels from $M_\infty = 0.74$ (fig. 29) to $M_\infty = 0.80$ (fig. 31). The NASA SC(2)-0012 and NACA 0012 pylons (which affected the lift characteristics of the model the most) caused greater flow disturbances than either the compression or hybrid pylons. The NASA SC(2)-0012 pylon appeared to cause the greatest extent of separation on the wing lower surface at $\eta = 0.375$, whereas the NACA 0012 pylon induced higher local velocities near the pylon for free-stream Mach numbers above 0.50, as indicated by the more negative pressure coefficients near $x/c = 0.30$. The wing loadings for all the pylon installations ($\eta = 0.400$) and for the clean wing are shown in figure 32. Once again, as was the case for the $\eta = 0.340$ pylon location, the compression pylon configuration affected the wing loading the least of the four pylon installations. The hybrid pylon did slightly better than either the NASA SC(2)-0012 pylon or the NACA 0012 pylon in terms of matching the clean wing loading.

Concluding Remarks

Pylon cross sections were investigated on a 1/17th-scale, low-wing transport model in the Langley 16-Foot Transonic Tunnel. A compression pylon and its hybrid derivative seem promising from the standpoint of better aerodynamic integration for the following reasons:

1. Flow acceleration can be alleviated without introducing severe adverse pressure gradients near the pylon-wing junction. The flow acceleration can be reduced by means of a gradually diverging pylon with maximum thickness at the wing trailing edge. The pylon trailing-edge closure (flow compression region) occurs aft of the wing trailing edge.
2. The resulting wing pressure distributions are close to those for the clean wing, which implies a small loss of lift and also minimal flow separation at the pylon-wing junction. Flow visualization data confirm the minimal separation.
3. The trends are similar for two different pylon locations on the wing.
4. Changes in pylon geometry (“airfoil shape”) have more influence on lift coefficient and pressure coefficient than minor variations in pylon toe-in angle (“airfoil angle of attack”).

Although this study of generic pylon cross sections has indicated some useful performance trends, the following important issues should be resolved:

1. The compression pylon, with its bulkier aft end and thinner forward end, poses a structural challenge for conventionally mounted forward engines. This problem is not as crucial for the hybrid pylon because it has a more uniform thickness distribution.
2. The nature and extent of the separated flow at the pylon-wing junction are crucial determinants of installation drag. However, high Reynolds number studies are needed because this kind of pressure-gradient-induced separation can be quite different at full-scale Reynolds numbers.
3. The compression pylon and hybrid pylon concepts should be tested with a nacelle attached because the presence of a nacelle can, depending on proximity, further compound or alleviate flow accelerations and gradients.
4. For nacelles very close to the wing and for very high bypass ratio nacelles, the effects of fan and core exhausts should be considered.
5. Three-dimensional inverse-design methods should be used to design pylon and fillet geometry from prescribed pressure distributions.

6. A pylon geometry might only be good at a single design point, whereas practical implementation can require geometry optimization for multipoint design.

NASA Langley Research Center
Hampton, VA 23681-0001
April 12, 1993

References

1. Pendergraft, Odis C., Jr.; Ingraldi, Anthony M.; Re, Richard J.; and Kariya, Timmy T.: *Installation Effects of Wing-Mounted Turbofan Nacelle-Pylons on a 1/17th-Scale, Twin-Engine, Low-Wing Transport Model*. NASA TP-3168, 1992.
2. Ingraldi, Anthony M.; Kariya, Timmy T.; and Re, Richard J.: Interference Effects of Very High Bypass Ratio Nacelle Installations on a Low-Wing Transport. ASME Paper 91-GT-241, June 1991.
3. Pendergraft, Odis C., Jr.; Ingraldi, Anthony M.; Re, Richard J.; and Kariya, Timmy T.: Nacelle/Pylon Interference Study on a 1/17th-Scale, Twin-Engine, Low-Wing Transport Model. AIAA-89-2480, July 1989.
4. Naik, D. A.; Chen, H. C.; Su, T. Y.; and Kao, T. J.: Euler Analysis of Turbofan/Superfan Integration for a Transport Aircraft. *Aerodynamic Engine/Airframe Integration for High Performance Aircraft and Missiles*, AGARD-CP-498 Sept. 1992, pp. 7-1-7-11.
5. Carlson, John R.; and Lamb, Milton: *Integration Effects of Pylon Geometry on a High-Wing Transport Airplane*. NASA TP-2877, 1989.
6. Corson, Blake W., Jr.; Runckel, Jack F.; and Igoe, William B.: *Calibration of the Langley 16-Foot Transonic Tunnel With Test Section Air Removal*. NASA TR R-423, 1974.
7. Staff of the Propulsion Aerodynamics Branch: *A User's Guide to the Langley 16-Foot Tunnel Complex, Revision 1*. NASA TM-102750, 1990.
8. Mineck, Raymond E.; and Lawing, Pierce L.: *High Reynolds Number Tests of the NASA SC(2)-0012 Airfoil in the Langley 0.3-Meter Transonic Cryogenic Tunnel*. NASA TM-89102, 1987.
9. Naik, Dinesh A.: Innovative Pylon Concepts for Engine-Airframe Integration for Transonic Transports. AIAA-89-1819, June 1989.
10. Mercer, Charles E.; Berrier, Bobby L.; Capone, Francis J.; Grayston, Alan M.; and Sherman, C. D.: *Computations for the 16-Foot Transonic Tunnel—NASA, Langley Research Center, Revision 1*. NASA TM-86319, 1987. (Supersedes NASA TM-86319, 1984.)

Table I. Coordinates of the Four Pylon Cross Sections

(a) NACA 0012 pylon

(b) NASA SC(2)-0012 pylon

Outboard/Inboard	
x/c'	y/c'
0.00000	0.00000
.00154	.00688
.00616	.01350
.01382	.01985
.02447	.02589
.03806	.03158
.05450	.03687
.07368	.04171
.09549	.04605
.11980	.04985
.14645	.05308
.17528	.05571
.20611	.05771
.23875	.05909
.27300	.05985
.30866	.06000
.34549	.05957
.38328	.05861
.42178	.05715
.46077	.05524
.50000	.05294
.53923	.05030
.57822	.04738
.61672	.04424
.65451	.04092
.69134	.03748
.72700	.03396
.76125	.03042
.79389	.02691
.82472	.02345
.85355	.02011
.88020	.01691
.90451	.01391
.92632	.01115
.94550	.00866
.96194	.00648
.97553	.00464
.98618	.00318
.99384	.00212
.99846	.00148
1.00000	.00126

Outboard/Inboard	
x/c'	y/c'
0.00000	0.00000
.00200	.00910
.00500	.01390
.01000	.01860
.02000	.02480
.03000	.02910
.04000	.03240
.05000	.03500
.06000	.03730
.07000	.03930
.08000	.04110
.09000	.04280
.10000	.04420
.11000	.04560
.12000	.04680
.13000	.04800
.14000	.04900
.15000	.05000
.16000	.05100
.17000	.05180
.18000	.05260
.19000	.05340
.20000	.05410
.21000	.05470
.22000	.05530
.23000	.05590
.24000	.05640
.25000	.05680
.26000	.05730
.27000	.05770
.28000	.05800
.29000	.05840
.30000	.05880
.31000	.05900
.32000	.05920

Outboard/Inboard	
x/c'	y/c'
0.33000	0.05950
.34000	.05960
.35000	.05970
.36000	.05980
.37000	.06000
.38000	.06000
.39000	.06000
.40000	.06000
.41000	.06000
.42000	.05980
.43000	.05970
.44000	.05960
.45000	.05950
.46000	.05920
.47000	.05900
.48000	.05880
.49000	.05840
.50000	.05800
.51000	.05770
.52000	.05730
.53000	.05680
.54000	.05640
.55000	.05580
.56000	.05520
.57000	.05460
.58000	.05380
.59000	.05310
.60000	.05230
.61000	.05130
.62000	.05040
.63000	.04930
.64000	.04820
.65000	.04700
.66000	.04580

Outboard/Inboard	
x/c'	y/c'
0.67000	0.04450
.68000	.04330
.69000	.04200
.70000	.04080
.71000	.03950
.72000	.03820
.73000	.03700
.74000	.03570
.75000	.03450
.76000	.03320
.77000	.03190
.78000	.03070
.79000	.02940
.80000	.02820
.81000	.02690
.82000	.02560
.83000	.02440
.84000	.02310
.85000	.02190
.86000	.02060
.87000	.01930
.88000	.01810
.89000	.01680
.90000	.01560
.91000	.01430
.92000	.01300
.93000	.01180
.94000	.01050
.95000	.00930
.96000	.00800
.97000	.00670
.98000	.00550
.99000	.00420
1.00000	.00300

Table I. Concluded

(c) Compression pylon

Outboard/Inboard	
x/c'	y/c'
0.00000	0.00000
.00130	.00670
.00500	.01170
.01090	.01520
.01880	.01740
.02830	.01870
.03940	.01950
.05000	.02000
.20570	.02660
.37190	.03360
.53820	.04060
.70440	.04760
.87070	.05460
.91150	.05620
.95220	.05770
.99300	.05850
1.03380	.05780
1.07450	.05410
1.11530	.04590
1.15610	.03320
1.18390	.02340
1.21170	.01360
1.23940	.00370
1.25000	.00000

(d) Hybrid pylon

Outboard		Inboard	
x/c'	y/c'	x/c'	y/c'
0.00000	0.00000	0.00000	0.00000
.00250	.01138	.00130	-.00670
.01250	.02325	.00500	-.01170
.03750	.03638	.01090	-.01520
.05205	.04105	.01880	-.01740
.07500	.04663	.02830	-.01870
.12155	.05478	.03940	-.01950
.19196	.06295	.04731	-.01990
.26265	.06839	.06244	-.02101
.33345	.07196	.19534	-.02623
.40430	.07412	.32821	-.03176
.47519	.07500	.46109	-.03736
.54607	.07454	.59396	-.04295
.61695	.07282	.72684	-.04865
.68778	.06974	.85971	-.05416
.75848	.06453	.99265	-.05753
.82893	.05674	1.05014	-.05746
.89926	.04784	1.09025	-.05094
.96960	.03903	1.12034	-.04434
1.03995	.03019	1.15042	-.03497
1.11028	.02129	1.20056	-.01749
1.18063	.01245	1.24370	-.00220
1.25000	.00000	1.25000	.00000

(a) Sketch showing geometry of pylons. All pylons were set back from the wing leading edge by 5 percent of the local wing chord.

Figure 3. Details of pylon installation.

(b) Lower surface.

Figure 12. Effect of compression pylons installed at $\eta = 0.340$ on wing static pressure coefficients for $M_\infty = 0.77$.

(a) $\eta = 0.310$.

Figure 14. Comparison of static pressure coefficients on wing lower surface of various configurations for $M_\infty = 0.50$ and $C_L \approx 0.55$ with pylons installed at $\eta = 0.340$.

(a) $\eta = 0.310$.

Figure 15. Comparison of static pressure coefficients on wing lower surface of various configurations for $M_\infty = 0.74$ and $C_L \approx 0.55$ with pylons installed at $\eta = 0.340$.

(a) $\eta = 0.310$.

Figure 16. Comparison of static pressure coefficients on wing lower surface of various configurations for $M_\infty = 0.77$ and $C_L \approx 0.55$ with pylons installed at $\eta = 0.340$.

(a) $\eta = 0.310$.

Figure 17. Comparison of static pressure coefficients on wing lower surface of various configurations for $M_\infty = 0.80$ and $C_L \approx 0.55$ with pylons installed at $\eta = 0.340$.

Figure 22. Comparison of lift characteristics for clean wing and for pylons installed at $\eta = 0.400$ with $M_\infty = 0.77$.

Figure 23. Comparison of lift characteristics for clean wing and for pylons installed at $\eta = 0.400$ with $M_\infty = 0.77$. Detail near $C_L = 0.55$.

Figure 26. Effect of compression pylons installed at $\eta = 0.400$ on wing static pressure coefficients for $M_\infty = 0.77$.

(a) $\eta = 0.375$.

Figure 28. Comparison of static pressure coefficients on wing lower surface of various configurations for $M_\infty = 0.50$ and $C_L \approx 0.55$ with pylons installed at $\eta = 0.400$.

(a) $\eta = 0.375$.

Figure 29. Comparison of static pressure coefficients on wing lower surface of various configurations for $M_\infty = 0.74$ and $C_L \approx 0.55$ with pylons installed at $\eta = 0.400$.

(a) $\eta = 0.375$.

Figure 30. Comparison of static pressure coefficients on wing lower surface of various configurations for $M_\infty = 0.77$ and $C_L \approx 0.55$ with pylons installed at $\eta = 0.400$.

(a) $\eta = 0.375$.

Figure 31. Comparison of static pressure coefficients on wing lower surface of various configurations for $M_\infty = 0.80$ and $C_L \approx 0.55$ with pylons installed at $\eta = 0.400$.

Figure 1. Fluorescent oil flow photograph of wing lower surface at $M_\infty = 0.77$ and $\alpha = 1^\circ$ for turbofan flow-through nacelle at $\eta = 0.340$.

(a) General characteristics. Linear dimensions are given in inches.

Figure 2. Basic low-wing transport model without nacelles.

L-91-00692

(b) Photograph of model without pylons installed in the Langley 16-Foot Transonic Tunnel.

Figure 2. Continued.

(c) Planform geometry. Linear dimensions are given in inches.

Figure 2. Concluded.

(a) Sketch showing geometry of pylons. All pylons were set back from the wing leading edge by 5 percent of the local wing chord.

Figure 3. Details of pylon installation.

L-91-00695

(b) Photograph of front view of model with compression pylons installed at $\eta = 0.340$.

Figure 3. Continued.

L-91-00696

(c) Photograph of rear view of model with compression pylons installed at $\eta = 0.340$.

Figure 3. Continued.

L-91-00699

(d) Close-up view of model with compression pylons installed at $\eta = 0.340$.

Figure 3. Concluded.

Figure 4. Sketch of wing showing orifice locations. Linear dimensions are given in inches.

(a) Wing locations.

Figure 5. Location of boundary-layer transition strips on model. Linear dimensions are given in inches.

(b) Fuselage nose location.

(c) Typical location of pylon transition grit.

Figure 5. Concluded.

(a) $M_\infty = 0.50$.

Figure 6. Effect of pylon toe-in angle on lift characteristics for pylons installed at $\eta = 0.340$.

(b) $M_\infty = 0.74$.

Figure 6. Continued.

(c) $M_\infty = 0.77$.

Figure 6. Continued.

(d) $M_\infty = 0.80$.

Figure 6. Concluded.

Figure 7. Effect of pylon toe-in angle on lift characteristics near the design point ($M_\infty = 0.77$ and $C_L = 0.55$) for pylons installed at $\eta = 0.340$.

Figure 8. Comparison of lift characteristics for clean wing and for pylons installed at $\eta = 0.340$ for $M_\infty = 0.77$.

Figure 9. Comparison of lift characteristics for clean wing and for pylons installed at $\eta = 0.340$ for $M_\infty = 0.77$. Detail is near $C_L = 0.55$.

(a) Upper surface.

(b) Lower surface.

Figure 10. Effect of NACA 0012 pylons installed at $\eta = 0.340$ on wing static pressure coefficients for $M_\infty = 0.77$. Semispan stations given to right of plot.

(a) Upper surface.

(b) Lower surface.

Figure 11. Effect of NASA SC(2)-0012 pylons installed at $\eta = 0.340$ on wing static pressure coefficients for $M_\infty = 0.77$.

(a) Upper surface.

(b) Lower surface.

Figure 12. Effect of compression pylons installed at $\eta = 0.340$ on wing static pressure coefficients for $M_\infty = 0.77$.

(a) Upper surface.

(b) Lower surface.

Figure 13. Effect of hybrid pylons installed at $\eta = 0.340$ on wing static pressure coefficients for $M_\infty = 0.77$.

(a) $\eta = 0.310$.

Figure 14. Comparison of static pressure coefficients on wing lower surface of various configurations for $M_\infty = 0.50$ and $C_L \approx 0.55$ with pylons installed at $\eta = 0.340$.

(b) $\eta = 0.375$.

Figure 14. Concluded.

(a) $\eta = 0.310$.

Figure 15. Comparison of static pressure coefficients on wing lower surface of various configurations for $M_\infty = 0.74$ and $C_L \approx 0.55$ with pylons installed at $\eta = 0.340$.

(b) $\eta = 0.375$.

Figure 15. Concluded.

(a) $\eta = 0.310$.

Figure 16. Comparison of static pressure coefficients on wing lower surface of various configurations for $M_\infty = 0.77$ and $C_L \approx 0.55$ with pylons installed at $\eta = 0.340$.

(b) $\eta = 0.375$.

Figure 16. Concluded.

(a) $\eta = 0.310$.

Figure 17. Comparison of static pressure coefficients on wing lower surface of various configurations for $M_\infty = 0.80$ and $C_L \approx 0.55$ with pylons installed at $\eta = 0.340$.

(b) $\eta = 0.375$.

Figure 17. Concluded.

L-91-7057

(a) Clean wing at $\alpha = 1.5^\circ$.

Figure 18. Fluorescent oil flow photographs of the wing lower surface of several configurations at $M_\infty = 0.50$ and $C_L = 0.55$.

L-91-7045

(b) NASA SC(2)-0012 pylon at $\alpha = 1.8^\circ$.

Figure 18. Continued.

L-91-7041

(c) Compression pylon at $\alpha = 1.6^\circ$.

Figure 18. Concluded.

L-91-7061

(a) Clean wing at $\alpha = 0.8^\circ$.

Figure 19. Fluorescent oil flow photographs of the wing upper surface of several configurations at $M_\infty = 0.77$ and $C_L = 0.55$.

L-91-7033

(b) NACA 0012 pylon at $\alpha = 1^\circ$.

Figure 19. Continued.

L-91-7036

(c) NASA SC(2)-0012 pylon at $\alpha = 1^\circ$.

Figure 19. Continued.

L-91-8657

(d) Compression pylon at $\alpha = 1^\circ$.

Figure 19. Concluded.

L-91-7059

(a) Clean wing at $\alpha = 0.8^\circ$.

Figure 20. Fluorescent oil flow photographs of the wing lower surface of several configurations at $M_\infty = 0.77$.

L-91-7043

(b) NASA SC(2)-0012 pylon at $\alpha = 1^\circ$.

Figure 20. Continued.

L-91-7052

(c) Compression pylon at $\alpha = 0.8^\circ$.

Figure 20. Concluded.

Figure 21. Variation of wing loading with span for various configurations at $M_\infty = 0.77$ with pylons installed at $\eta = 0.340$.

Figure 22. Comparison of lift characteristics for clean wing and for pylons installed at $\eta = 0.400$ with $M_\infty = 0.77$.

Figure 23. Comparison of lift characteristics for clean wing and for pylons installed at $\eta = 0.400$ with $M_\infty = 0.77$. Detail near $C_L = 0.55$.

(a) Upper surface.

(b) Lower surface.

Figure 24. Effect of NACA 0012 pylons installed at $\eta = 0.400$ on wing static pressure coefficients for $M_\infty = 0.77$.

(a) Upper surface.

(b) Lower surface.

Figure 25. Effect of NASA SC(2)-0012 pylons installed at $\eta = 0.400$ on wing static pressure coefficients for $M_\infty = 0.77$.

(a) Upper surface.

(b) Lower surface.

Figure 26. Effect of compression pylons installed at $\eta = 0.400$ on wing static pressure coefficients for $M_\infty = 0.77$.

(a) Upper surface.

(b) Lower surface.

Figure 27. Effect of hybrid pylons installed at $\eta = 0.400$ on wing static pressure coefficients for $M_\infty = 0.77$.

(a) $\eta = 0.375$.

Figure 28. Comparison of static pressure coefficients on wing lower surface of various configurations for $M_\infty = 0.50$ and $C_L \approx 0.55$ with pylons installed at $\eta = 0.400$.

(b) $\eta = 0.428$.

Figure 28. Concluded.

(a) $\eta = 0.375$.

Figure 29. Comparison of static pressure coefficients on wing lower surface of various configurations for $M_\infty = 0.74$ and $C_L \approx 0.55$ with pylons installed at $\eta = 0.400$.

(b) $\eta = 0.428$.

Figure 29. Concluded.

(a) $\eta = 0.375$.

Figure 30. Comparison of static pressure coefficients on wing lower surface of various configurations for $M_\infty = 0.77$ and $C_L \approx 0.55$ with pylons installed at $\eta = 0.400$.

(b) $\eta = 0.428$.

Figure 30. Concluded.

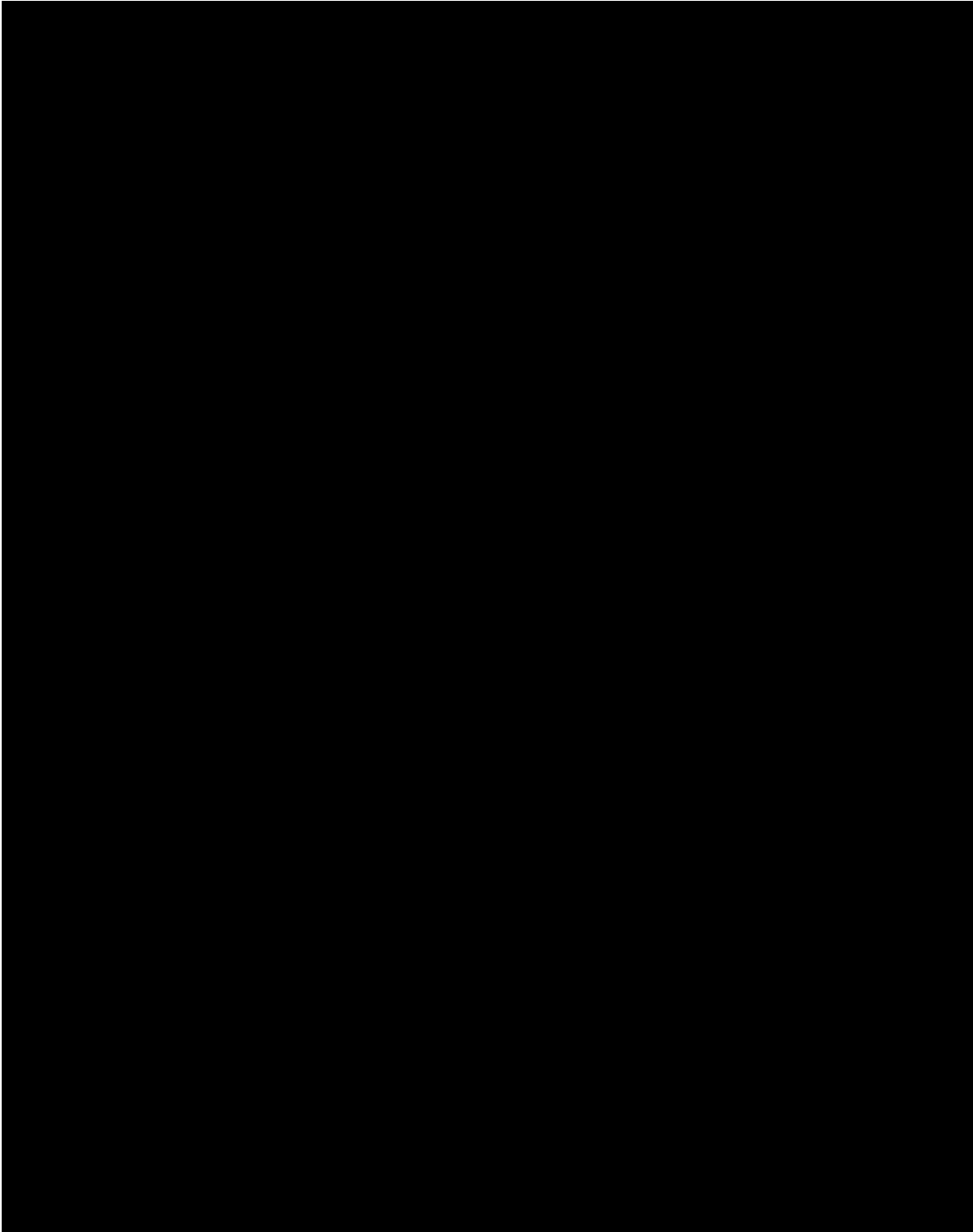
(a) $\eta = 0.375$.

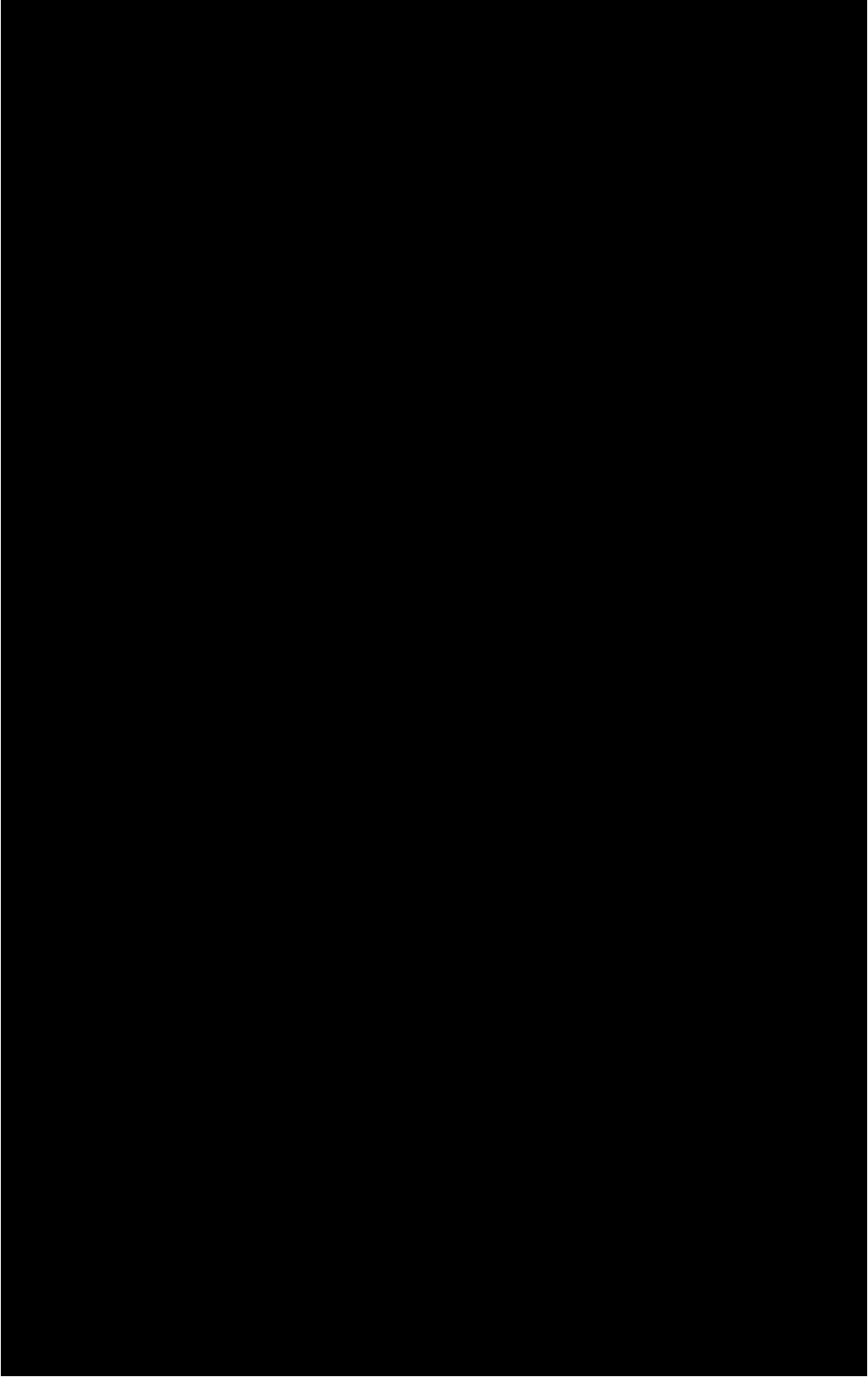
Figure 31. Comparison of static pressure coefficients on wing lower surface of various configurations for $M_\infty = 0.80$ and $C_L \approx 0.55$ with pylons installed at $\eta = 0.400$.

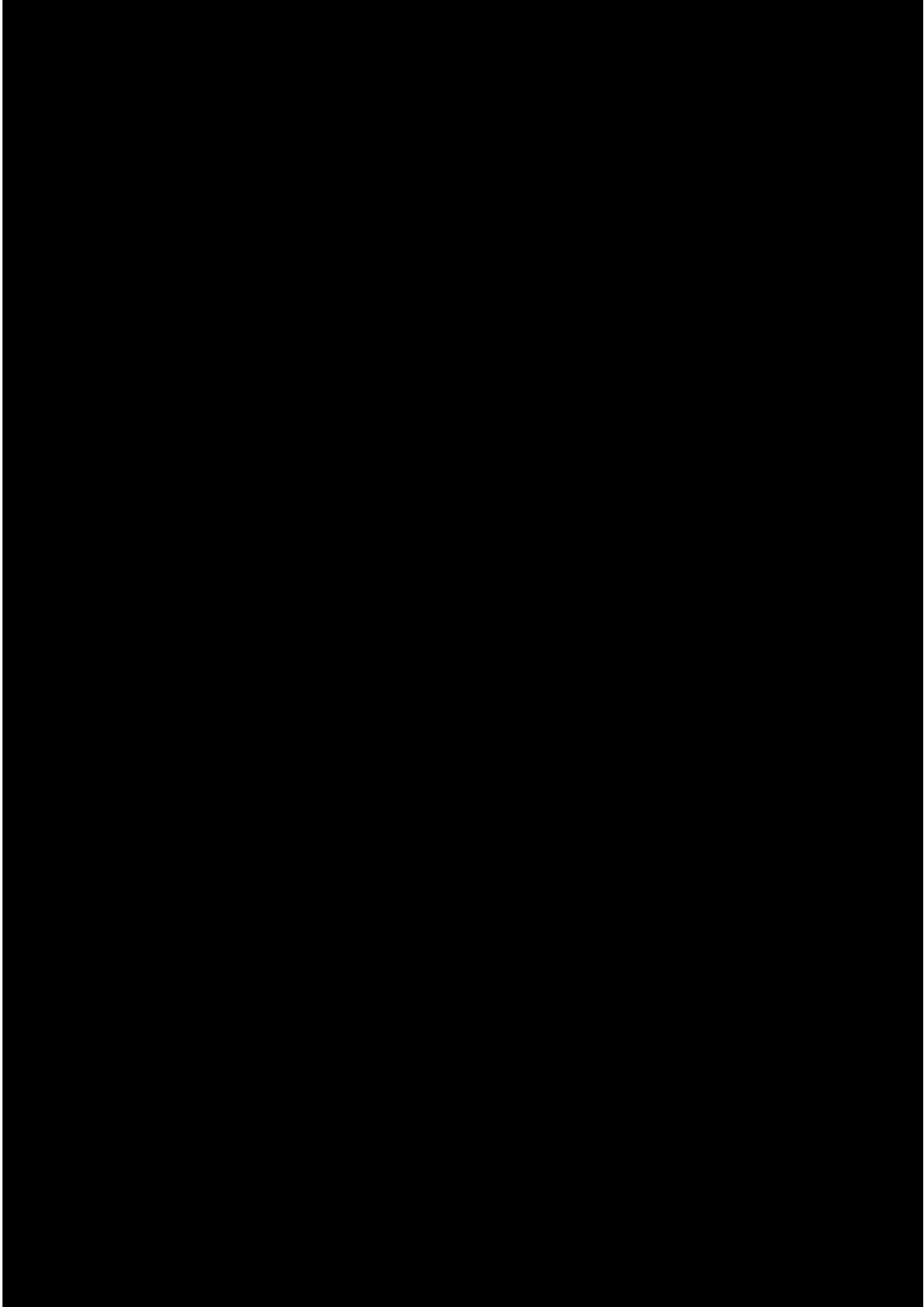
(b) $\eta = 0.428$.

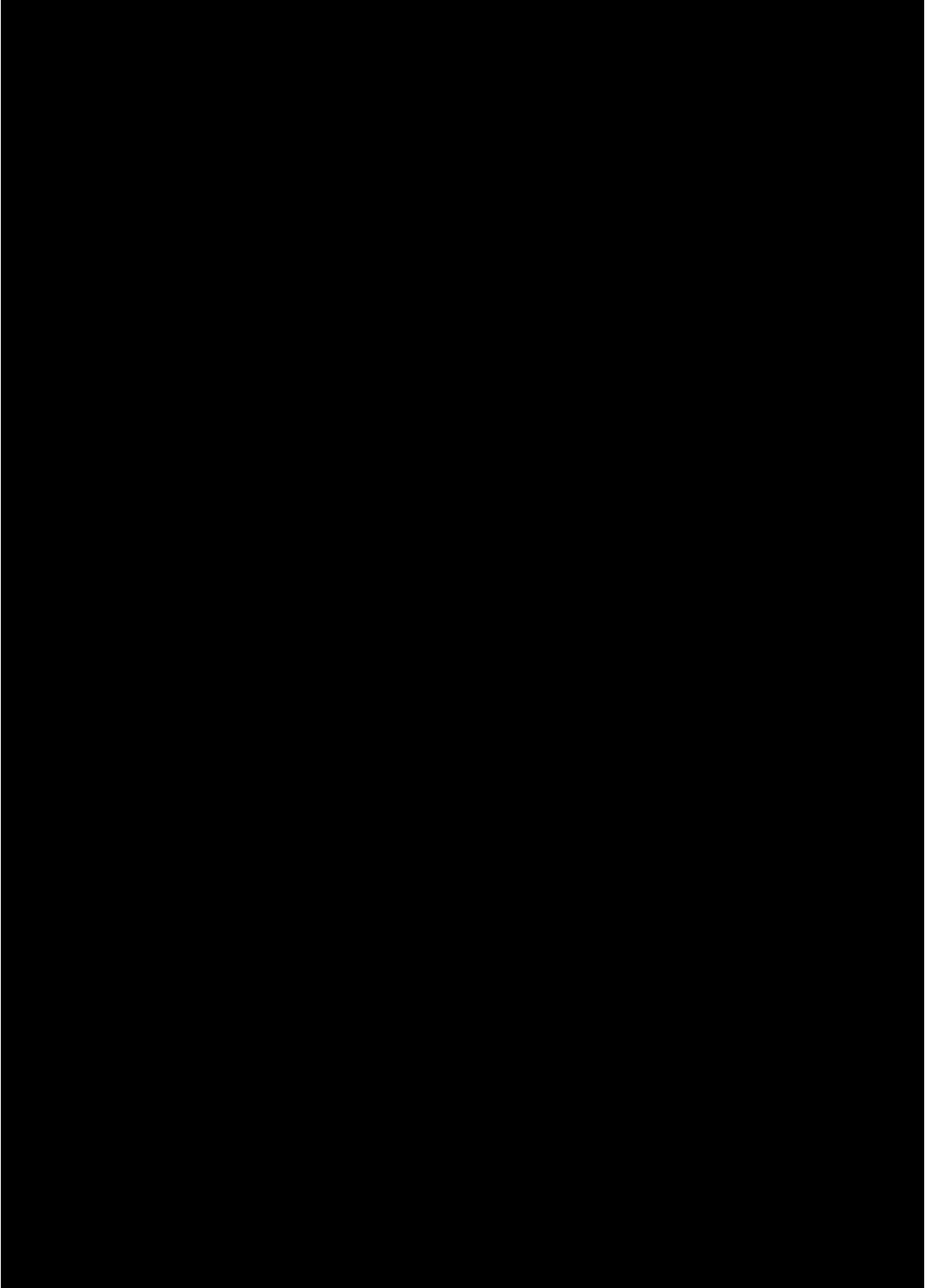
Figure 31. Concluded.

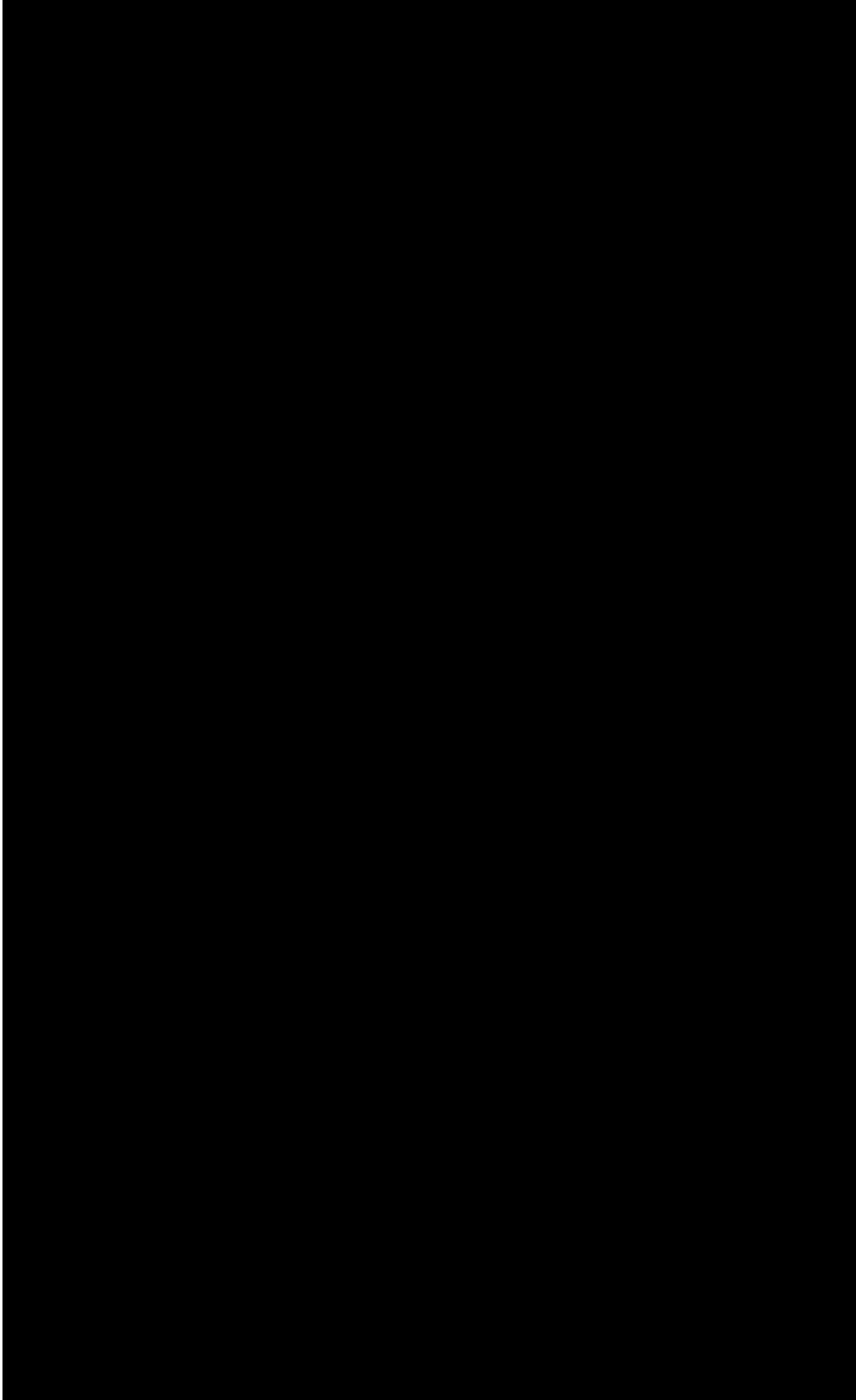
Figure 32. Variation of wing loading with span for various configurations at $M_\infty = 0.77$ with pylons installed at $\eta = 0.400$.

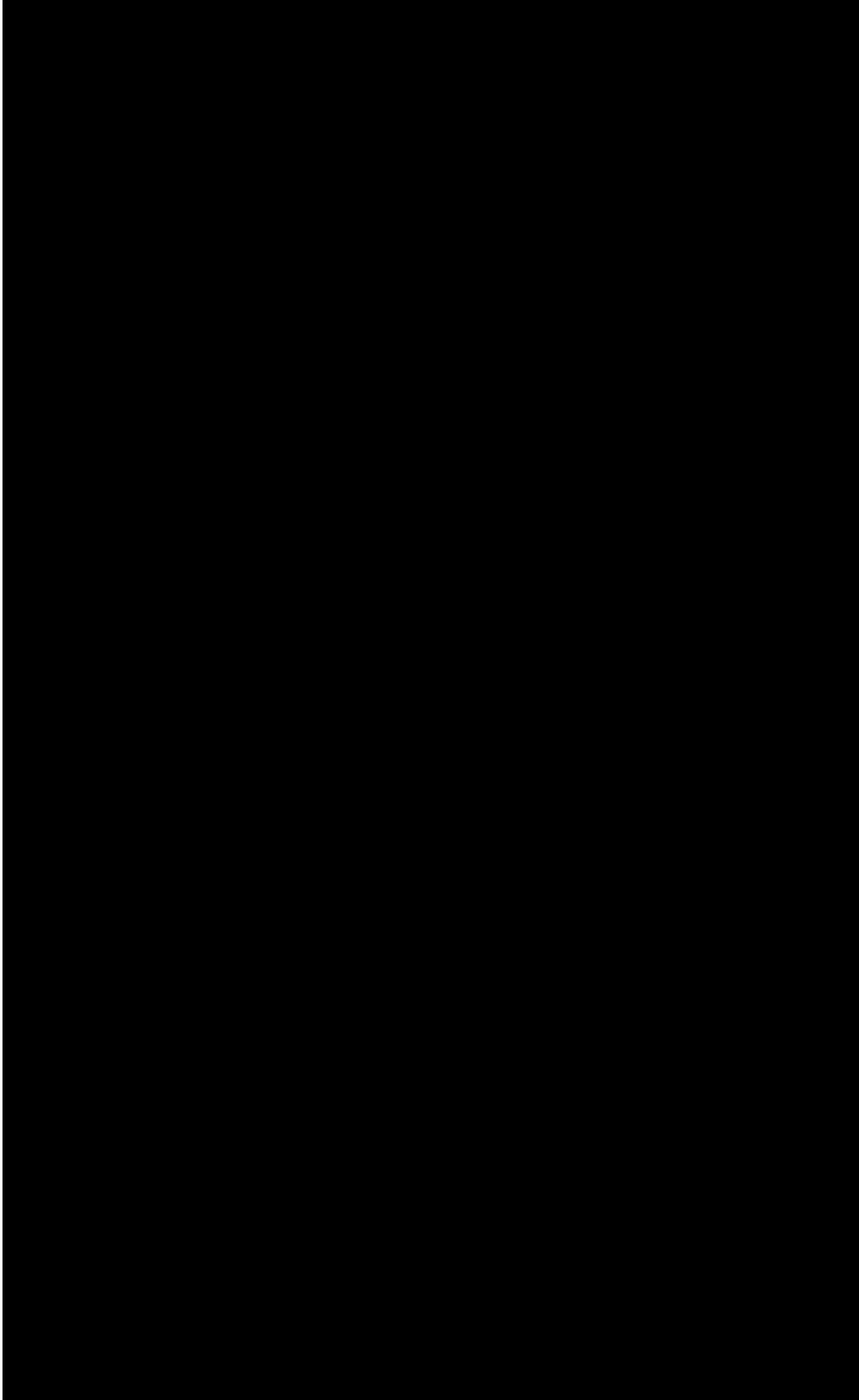


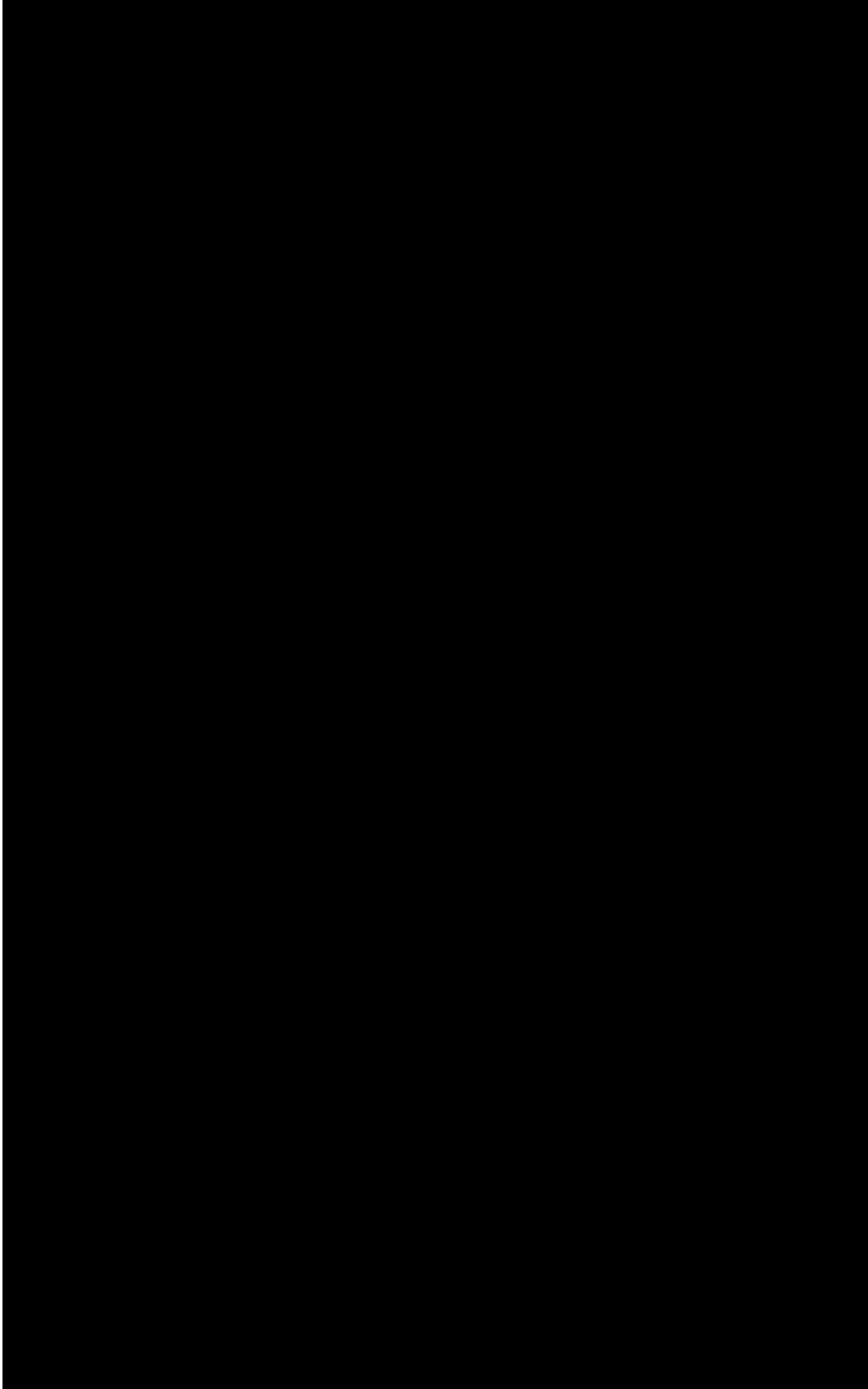


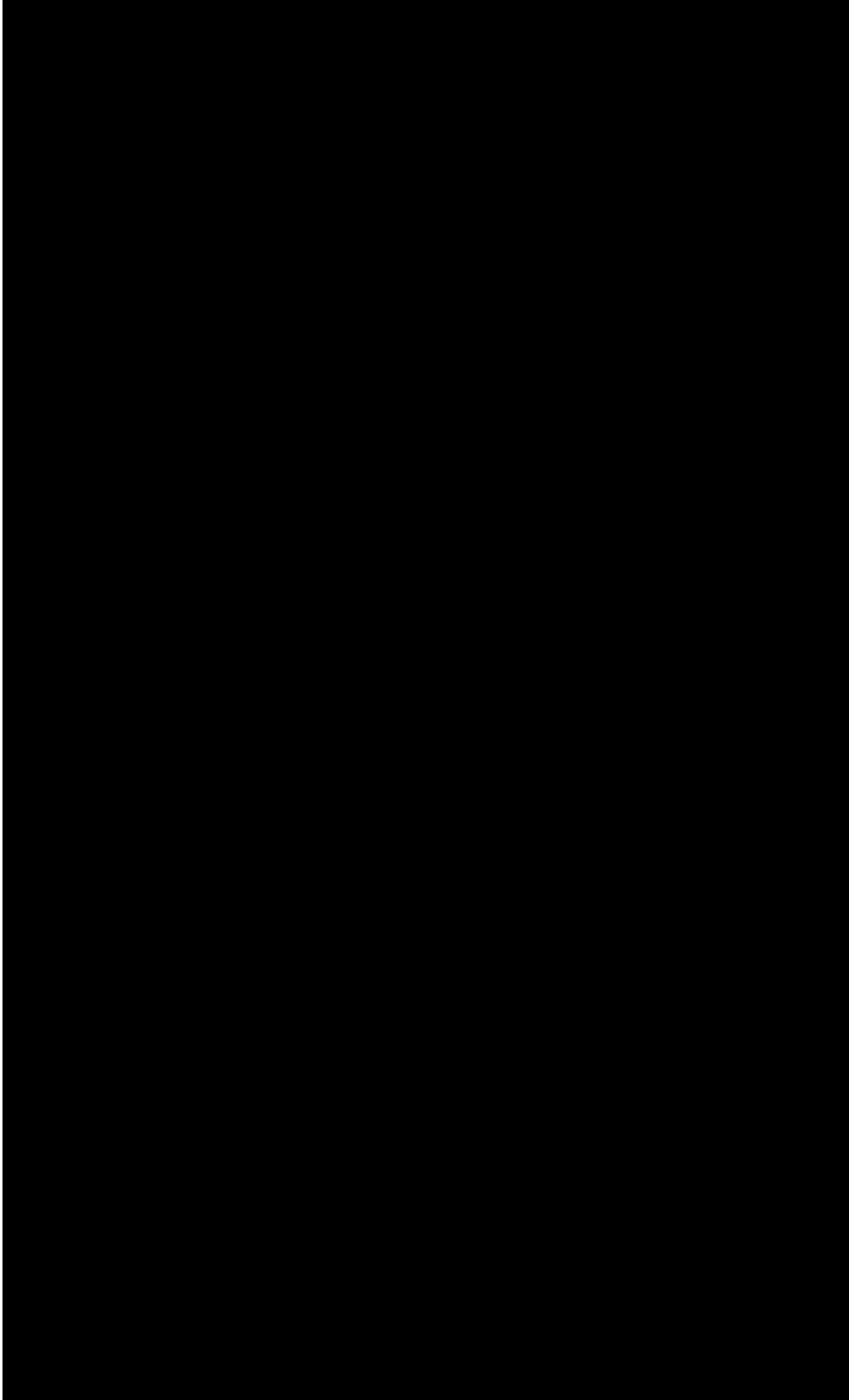


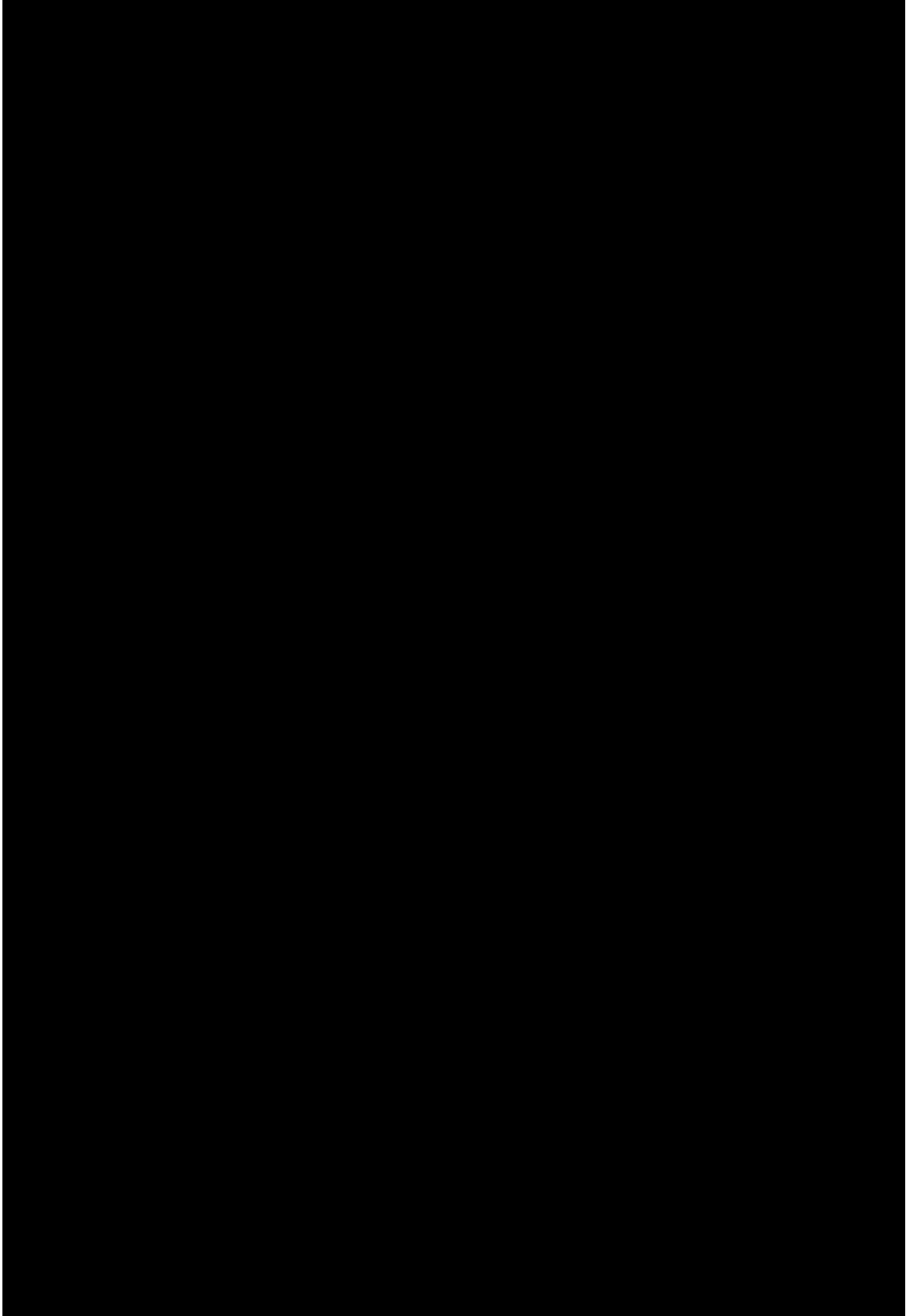


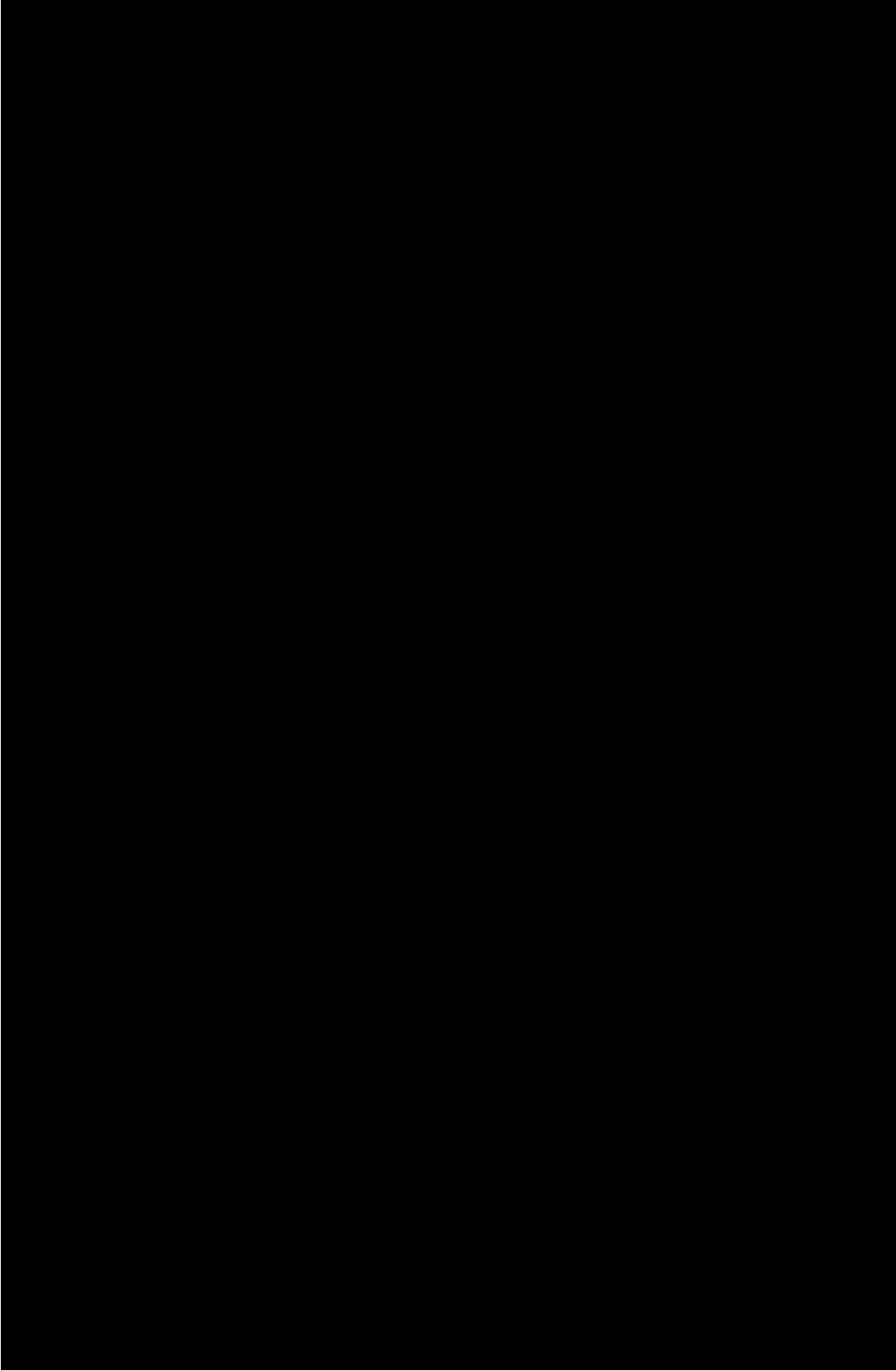


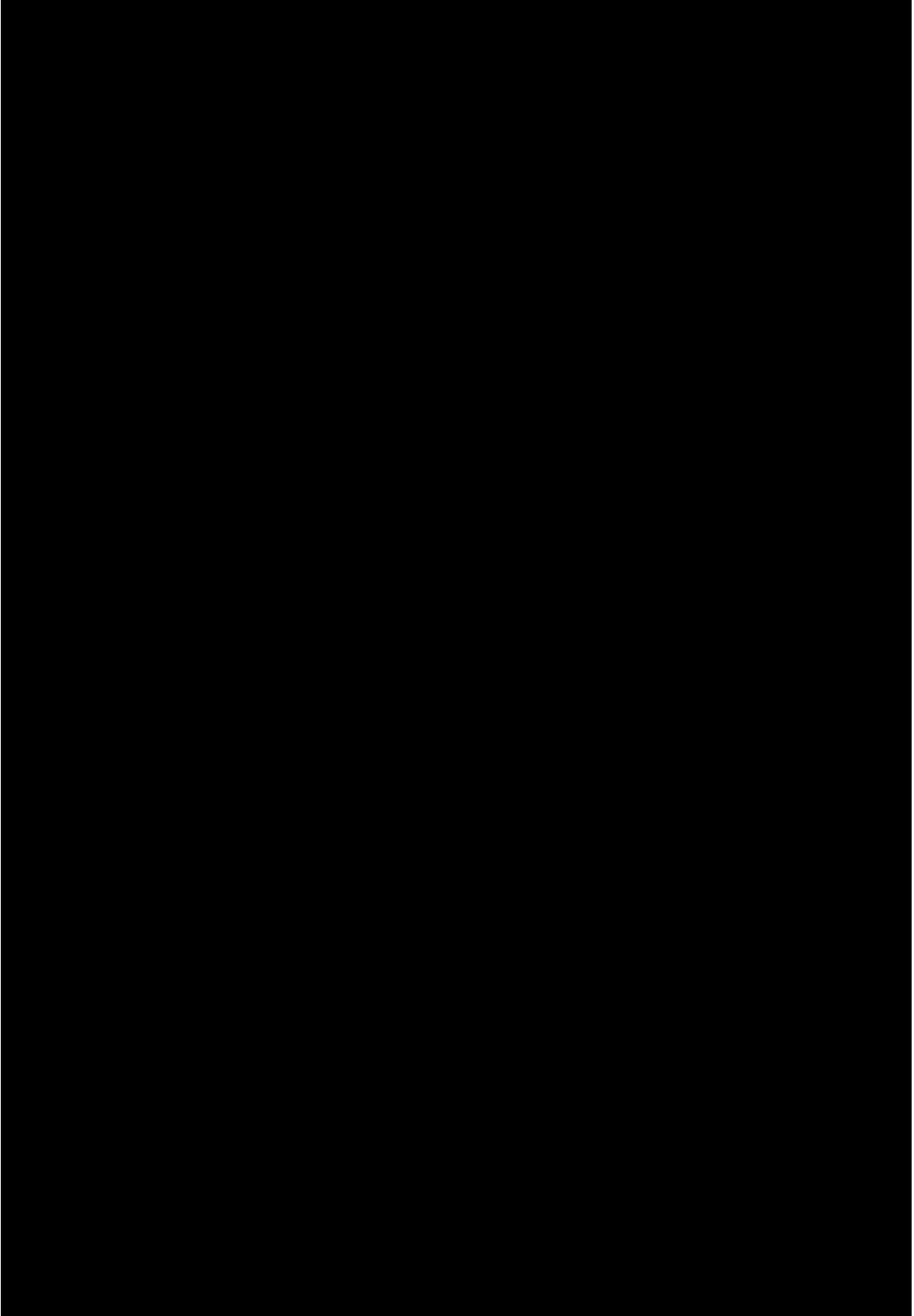












REPORT DOCUMENTATION PAGE			Form Approved OMB No. 0704-0188	
Public reporting burden for this collection of information is estimated to average 1 hour per response, including the time for reviewing instructions, searching existing data sources, gathering and maintaining the data needed, and completing and reviewing the collection of information. Send comments regarding this burden estimate or any other aspect of this collection of information, including suggestions for reducing this burden, to Washington Headquarters Services, Directorate for Information Operations and Reports, 1215 Jefferson Davis Highway, Suite 1204, Arlington, VA 22202-4302, and to the Office of Management and Budget, Paperwork Reduction Project (0704-0188), Washington, DC 20503.				
1. AGENCY USE ONLY (Leave blank)	2. REPORT DATE June 1993	3. REPORT TYPE AND DATES COVERED Technical Paper		
4. TITLE AND SUBTITLE Effect of Pylon Cross-Sectional Geometries on Propulsion Integration for a Low-Wing Transport			5. FUNDING NUMBERS WU 535-03-10-01	
6. AUTHOR(S) Anthony M. Ingraldi, Dinesh A. Naik, and Odis C. Pendergraft, Jr.				
7. PERFORMING ORGANIZATION NAME(S) AND ADDRESS(ES) NASA Langley Research Center Hampton, VA 23681-0001			8. PERFORMING ORGANIZATION REPORT NUMBER L-17149	
9. SPONSORING/MONITORING AGENCY NAME(S) AND ADDRESS(ES) National Aeronautics and Space Administration Washington, DC 20546-0001			10. SPONSORING/MONITORING AGENCY REPORT NUMBER NASA TP-3333	
11. SUPPLEMENTARY NOTES Ingraldi and Pendergraft: Langley Research Center, Hampton, VA; Naik: ViGYAN, Inc., Hampton, VA.				
12a. DISTRIBUTION/AVAILABILITY STATEMENT Unclassified-Unlimited Subject Category 02			12b. DISTRIBUTION CODE	
13. ABSTRACT (Maximum 200 words) An experimental program was conducted in the Langley 16-Foot Transonic Tunnel to evaluate the performance effects of various types of pylons on a 1/17th-scale, low-wing transport model. The model wing was designed for cruise at a Mach number of 0.77 and a lift coefficient of 0.55. The pylons were tested at two wing semispan locations over a range of toe-in angles. The effects of toe-in angle were found to be minimal, but the variation in geometry had a more pronounced effect on the lift characteristics of the model. A pylon whose maximum thickness occurred at the wing trailing edge, known as a compression pylon, proved to be the best choice in terms of retaining the flow characteristics of the wing without pylons. Practical considerations such as structural viability may necessitate modification of the compression pylon concept in order to take advantage of its apparent benefits.				
14. SUBJECT TERMS Pylon geometry; Transport aircraft; Propulsion integration; Installation under wing; Swept supercritical wing			15. NUMBER OF PAGES 64	
			16. PRICE CODE A04	
17. SECURITY CLASSIFICATION OF REPORT Unclassified	18. SECURITY CLASSIFICATION OF THIS PAGE Unclassified	19. SECURITY CLASSIFICATION OF ABSTRACT	20. LIMITATION OF ABSTRACT	